AIAA SciTech Forum
7-11 January 2019, San Diego, California
AIAA Scitech 2019 Forum

10.2514/6.2019-0219

Nonlinear Aeroelasticity of Morphing Wings with Corrugated Structures

Natsuki Tsushima[1] and Hitoshi Arizono[2]
Japan Aerospace Exploration Agency, Mitaka, Tokyo, 181-0015, Japan

Tomohiro Yokozeki[3]
The University of Tokyo, Hongo, Tokyo, 113-8656, Japan

Weihua Su[4]
The University of Alabama, Tuscaloosa, AL, 35487-0280

This paper consists of two main parts: 1) an enhancement of the integrated static aeroelastic framework developed in the previous works with dynamic analysis capability with a fully unsteady aerodynamic solver, and 2) a study of aeroelastic characteristics of morphing wings with corrugated structures to evaluate the aeroelastic performance. In the dynamic aeroelastic analysis framework, dynamic inertial effects are considered by taking into account the virtual work due to inertial forces. The time integration of the derived nonlinear equation of motion is performed by using the modified generalized-α improved for aeroelastic problems. In addition, the spring element is implemented in the structural solver for additional modeling capability. Verifications of the accommodation for dynamic analysis and a demonstration of the capability of the present dynamic aeroelastic analysis framework are performed. Numerical studies explore the static behaviors and performance of corrugated morphing wings by comparing with conventional wings using hinged flaps. This work allows to better understand the nonlinear aeroelastic characteristics of composite and corrugated morphing wings and demonstrates the feasibility of the methodology to simulate such morphing wings numerically.

I. Introduction

RECENTLY, wing morphing has generated a good deal of attention as a potential technique to improve aircraft performance and to facilitate economic flight. The morphing technique can achieve the optimal flight performance in a wide range of operation conditions by adaptively changing the wing shape, even in flight conditions in which conventional control surfaces decrease their performance. Specifically, the morphing technology may improve aerodynamic characteristics and reduce structural weight and acoustic noise of aircraft [1-4]. In addition, it may help to improve flight safety through enhancement of stall characteristics and gust alleviation.

The increasing population of global transportation and tighter economic restrictions contribute to the demand for improvements in aircraft performance. This demand has led aircraft engineers to environment-friendly design with low fuel consumption. Previously, as technologies to reduce fuel consumption, improvement of aerodynamic performance and weight reduction by enhancing the traditional wing design and integrating composite materials have been achieved. However, the development of the traditional design has been matured, and other technologies that may bring revolutionary changes to aircraft structures are strongly desired.

Many researchers have studied various morphing technologies to evaluate the performance of those morphing wings. One of the contemporary concepts taking advantage of such wing morphing technique is the Variable Camber Continuous Trailing Edge Flap (VCCTEF) system [4, 5]. The VCCTEF adopted a flap system which was capable of changing flap angles in spanwise direction seamlessly. In addition, the system implemented three discrete control surface sections in chordwise direction contributing to distribute chordwise aerodynamic pressures smoothly.

[1] Researcher (tsushima.natsuki@jaxa.jp), Aeronautical Technology Directorate, Student Member AIAA.
[2] Researcher (arizono.hitoshi@jaxa.jp), Aeronautical Technology Directorate, Senior Member AIAA.
[3] Associate Professor (yokozeki@aastr.t.u-tokyo.ac.jp), Dept. of Aeronautics and Astronautics, Member AIAA.
[4] Associate Professor (suw@eng.ua.edu), Dept. of Aerospace Engineering and Mechanics, Senior Member AIAA.

The performance of the VCCTEF system was evaluated based on aerodynamic numerical simulations and wind tunnel tests, and the results showed performance improvements with respect to drag reduction and high-lift up to 6.31%.

Examples of morphing wing technologies include conceptual designs utilizing smart materials corresponding to recent developments in smart structures and materials technologies. For instance, Adaptive Compliant Trailing Edge (ACTE) flap [2, 3] was designed and tested by advantageously using the morphing concept and smart materials. The flaps can be actuated with piezoelectric materials, and the increase of lift and pitch moment owing to the ACTE flap has been proven in flight tests. Such piezoelectric-based morphing wings have the two advantages of fast response and high bandwidth. Morphing wings with piezoelectric materials are suitable to suppress aeroelastic instabilities and can extend the flight envelope [6, 7]. In addition, the piezoelectric materials, which convert energies between mechanical and electrical forms, can also provide additional energy from wing vibrations [8]. More recently, spanwise adaptive wings using shape memory alloy (SMA) actuators for Prototype-Technology Evaluation Research Aircraft (PTERA) was developed [9]. Flight tests of the aircraft demonstrated a capability of adaptive wing actuation with the smart materials in flight. However, more understanding and properly designed actuating mechanism are needed to achieve practical and efficient application of such innovative aircraft with smart materials. A design problem involving multiple subsystems and functions requires to find the optimum balance between those functions. Such aeroelastic or aeroservoelastic design problems have been addressed with various multi-objective optimization algorithms [10-12]. An excellent review of the integrated aeroservoelastic design optimization focusing on aircraft and control systems of fixed-wing vehicles without aerodynamic heating can be found in Ref. [13], while Du et al. [14] examined an aerothermoelastic optimization problem with the existence of uncertainty in heat flux.

At the same time, another morphing wing strategy using a simple wiring actuation mechanism with corrugated structures has been studied [15-17]. Due to the anisotropy, corrugated structures are stiffer in one direction and softer in another direction. The dual functions of a morphing wing, including spanwise load bearing and chordwise morphing, are therefore possible by taking advantage of the extremely anisotropic property of corrugated structures. One advantage of the corrugated morphing scheme is that it is easy to fabricate corrugated structures. Additionally, corrugated structures can be actuated simply with commercially available actuators and wires although other driving methods may also be adopted. Improvement of aerodynamic characteristics and adaptivity to flight condition with the corrugated-based camber morphing should be evaluated properly. Energy to drive such wings also needs to be investigated.

Morphing technology aims to very efficient aerodynamic and structural designs (configuration) during flight, contributing to the high performance of aircraft. The morphing wing actively changes its geometry during flight and may undergo large deformations, but small strains, resulting in geometrically nonlinear deformations, limit-cycle oscillations (LCOs), and so on. Hence, to accurately analyze morphing aircraft/wings, an aeroelastic model to consider the geometrical nonlinearities is important. Even though the accurate nonlinear aeroelastic analysis can be performed by using computational fluid dynamics (CFD) [18-20], it compromises computational efficiency, especially in case the large wing motion is involved. As an alternative approach, an unsteady aerodynamic model can be coupled with a geometrically nonlinear finite element model for computational efficiency with adequately accurate solutions, which can be used for preliminary to middle stage of developments. Especially among different aerodynamic models used for problems subjected to the large deformations, an unsteady vortex-lattice method has shown to provide simplicity for implementation and computational cost reduction [21, 22].

In this paper, the integrated static aeroelastic analysis framework developed in the previous works has been extended to dynamic analysis framework to fully utilize the unsteady aerodynamic solver and analyze the nonlinear, unsteady aeroelastic response of morphing wing with composite structures. In the dynamic aeroelastic analysis framework, dynamic inertial effects are considered by taking into account the virtual work due to inertia forces. The time integration of the derived nonlinear equation of motion is performed by using the modified generalized-α improved for aeroelastic problems. In addition, the spring element is implemented in the structural solver for additional modeling capability. This paper demonstrates the feasibility and capability of the updated nonlinear, unsteady aeroelastic framework, which allows studying the aeroelastic response and performance of flexible and/or morphing wings subject to large deformations due to wing morphing.

II. Theoretical Formulation

A geometrically nonlinear static aeroelastic analysis framework, which has been developed in the previous works [23], is accommodated for dynamic analysis by using an approach introduced in Ref. [24]. In the aeroelastic analysis framework, a shell finite element, which can model thin wings, has been accommodated to model isotropic,

orthotropic, and corrugated plate-like structures. A corotational approach is used to model the impact of geometrical nonlinearity due to large deformation produced by wing morphing. An unsteady vortex-lattice aerodynamic method (UVLM) [25] has been implemented to couple with the structural model subject to the large deformation. A homogenization method to model a corrugated panel as an equivalent orthotropic plate has also been implemented. The nonlinear structural dynamics is solved using three-node triangular shell element by a superposition of the optimal triangle membrane (OPT) and discrete Kirchhoff triangle (DKT) elements. An overview of the formulation related to the accommodation for dynamic analysis is described below.

A. Velocities and Accelerations

The position vector $\mathbf{X}$ of a point P in a structure with respect to the global frame G as shown in Fig. 1 is expressed as

$$\mathbf{X} = \mathbf{X}^{\mathbf{G}} + \mathbf{T}_{\mathbf{GB}}\mathbf{x}_{\mathbf{P}}^{\mathbf{B}} \tag{1}$$

where $\mathbf{X}^{\mathbf{G}}$ is the position vector of the origin of the body frame B describing rigid body motion of the structure in the global frame, $\mathbf{x}_{\mathbf{P}}^{\mathbf{B}}$ is the position vector of *P* in the body frame, and $\mathbf{T}_{\mathbf{GB}}$ is a transformation matrix from the body frame to the global frame [23].

The position vector of *P* can also be expressed in the body as

$$\mathbf{x}_{\mathbf{P}}^{\mathbf{B}} = \mathbf{X}^{\mathbf{B}} + \mathbf{T}_{\mathbf{BE}_0}\left(\mathbf{x}_{\mathbf{e}} + \mathbf{d}_{\mathbf{e}}\right) \tag{2}$$

where $\mathbf{X}^{\mathbf{B}}$ is the position vector of the origin of the initial (undeformed) element coordinate $\mathbf{E_0}$, $\mathbf{T_{BE0}}$ is the transformation matrix from the initial element coordinate to the body frame, $\mathbf{x_e}$ and $\mathbf{d_e}$ are the position and displacement vectors in the initial element coordinate. Therefore, the position vector of *P* can be rewritten as

$$\mathbf{X} = \mathbf{X}^{\mathbf{G}} + \mathbf{T}_{\mathbf{GB}}\mathbf{X}^{\mathbf{B}} + \mathbf{T}_{\mathbf{GB}}\mathbf{T}_{\mathbf{BE}_0}\left(\mathbf{x}_{\mathbf{e}} + \mathbf{d}_{\mathbf{e}}\right) \tag{3}$$

The time derivative of the transformation matrix $\mathbf{T_{GE}}$ is

$$\dot{\mathbf{T}}_{\mathbf{GB}} = \boldsymbol{\Omega}\mathbf{T}_{\mathbf{GB}} \tag{4}$$

where $\boldsymbol{\Omega}$ is a skew-symmetric matrix of the prescribed angular velocity vector of the origin of the body frame. The velocity and acceleration vectors of the point *P* can be described as

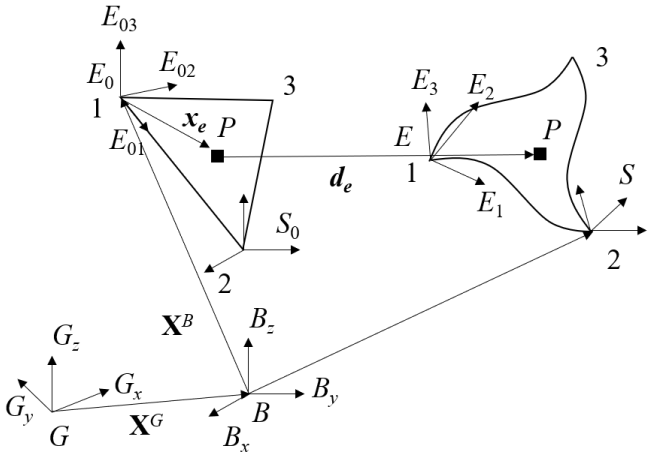

Figure 1. System frames of the triangular element.

$$\dot{\mathbf{X}} = \dot{\mathbf{X}}^{\mathbf{G}} + \boldsymbol{\Omega}\mathbf{T}_{\mathbf{GB}}\mathbf{X}^{\mathbf{B}} + \boldsymbol{\Omega}\mathbf{T}_{\mathbf{GB}}\mathbf{T}_{\mathbf{BE_0}}\left(\mathbf{x_e} + \mathbf{d_e}\right) + \mathbf{T}_{\mathbf{GB}}\mathbf{T}_{\mathbf{BE_0}}\dot{\mathbf{d}}_{\mathbf{e}} \tag{5}$$

$$\ddot{\mathbf{X}} = \ddot{\mathbf{X}}^{\mathbf{G}} + \left(\dot{\boldsymbol{\Omega}} + \boldsymbol{\Omega}\boldsymbol{\Omega}\right)\mathbf{T}_{\mathbf{GB}}\left[\mathbf{X}^{\mathbf{B}} + \mathbf{T}_{\mathbf{BE_0}}\left(\mathbf{x_e} + \mathbf{d_e}\right)\right] + 2\boldsymbol{\Omega}\mathbf{T}_{\mathbf{GB}}\mathbf{T}_{\mathbf{BE_0}}\dot{\mathbf{d}}_{\mathbf{e}} + \mathbf{T}_{\mathbf{GB}}\mathbf{T}_{\mathbf{BE_0}}\ddot{\mathbf{d}}_{\mathbf{e}} \tag{6}$$

B. Virtual Work due to Inertias

The virtual work done on an element due to the inertial force for each element is obtained by

$$\delta W = \rho_e \int_{V_{el}} \boldsymbol{\delta}\mathbf{X}^{\mathbf{T}}\ddot{\mathbf{X}} dV_{el} \tag{7}$$

where ρ_e and V_{el} are the density and volume of the element. The variation of the position vector $\boldsymbol{\delta}\mathbf{X}$, can be written as

$$\boldsymbol{\delta}\mathbf{X} = \mathbf{T}_{\mathbf{GB}}\mathbf{T}_{\mathbf{BE_0}}\boldsymbol{\delta}\mathbf{d}_{\mathbf{e}} \tag{8}$$

By using a matrix of shape functions $\mathbf{N}$ and a nodal degree of freedom $\mathbf{q}$ in the initial element coordinate, the displacement vector $\mathbf{d_e}$ can be computed as

$$\mathbf{d_e} = \mathbf{Nq} \tag{9}$$

Therefore, by substituting Eqs. (6) and (8) with Eq. (9) into Eq. (7), the virtual work due to the inertial forces can be expressed as

$$\begin{aligned}\delta W = \rho_e \int_{V_{el}} \{&\boldsymbol{\delta}\mathbf{q}^{\mathbf{T}}\mathbf{N}^{\mathbf{T}}\mathbf{T}_{\mathbf{BE_0}}^{\mathbf{T}}\mathbf{T}_{\mathbf{GB}}^{\mathbf{T}}\ddot{\mathbf{X}}^{\mathbf{G}} + \boldsymbol{\delta}\mathbf{q}^{\mathbf{T}}\mathbf{N}^{\mathbf{T}}\mathbf{T}_{\mathbf{BE_0}}^{\mathbf{T}}\mathbf{T}_{\mathbf{GB}}^{\mathbf{T}}\left(\dot{\boldsymbol{\Omega}} + \boldsymbol{\Omega}\boldsymbol{\Omega}\right)\mathbf{T}_{\mathbf{GB}}\mathbf{X}^{\mathbf{B}} \\ &+\boldsymbol{\delta}\mathbf{q}^{\mathbf{T}}\mathbf{N}^{\mathbf{T}}\mathbf{T}_{\mathbf{BE_0}}^{\mathbf{T}}\mathbf{T}_{\mathbf{GB}}^{\mathbf{T}}\left(\dot{\boldsymbol{\Omega}} + \boldsymbol{\Omega}\boldsymbol{\Omega}\right)\mathbf{T}_{\mathbf{GB}}\mathbf{T}_{\mathbf{BE_0}}\mathbf{x_e} + \boldsymbol{\delta}\mathbf{q}^{\mathbf{T}}\mathbf{N}^{\mathbf{T}}\mathbf{T}_{\mathbf{BE_0}}^{\mathbf{T}}\mathbf{T}_{\mathbf{GB}}^{\mathbf{T}}\left(\dot{\boldsymbol{\Omega}} + \boldsymbol{\Omega}\boldsymbol{\Omega}\right)\mathbf{T}_{\mathbf{GB}}\mathbf{T}_{\mathbf{BE_0}}\mathbf{Nq} \\ &+2\boldsymbol{\delta}\mathbf{q}^{\mathbf{T}}\mathbf{N}^{\mathbf{T}}\mathbf{T}_{\mathbf{BE_0}}^{\mathbf{T}}\mathbf{T}_{\mathbf{GB}}^{\mathbf{T}}\boldsymbol{\Omega}\mathbf{T}_{\mathbf{GB}}\mathbf{T}_{\mathbf{BE_0}}\mathbf{N}\dot{\mathbf{q}} + \boldsymbol{\delta}\mathbf{q}^{\mathbf{T}}\mathbf{N}^{\mathbf{T}}\mathbf{T}_{\mathbf{BE_0}}^{\mathbf{T}}\mathbf{T}_{\mathbf{GB}}^{\mathbf{T}}\mathbf{T}_{\mathbf{GB}}\mathbf{T}_{\mathbf{BE_0}}\mathbf{N}\ddot{\mathbf{q}}\ \}dV_{el}\end{aligned} \tag{10}$$

According to Eq. (10), the element local mass, gyroscopic damping, and dynamic stiffness matrices, and inertial force vector are

$$\mathbf{M}^{\mathbf{el}} = \rho_e \int_{V_{el}} \left\{\mathbf{N}^{\mathbf{T}}\mathbf{T}_{\mathbf{BE_0}}^{\mathbf{T}}\mathbf{T}_{\mathbf{GB}}^{\mathbf{T}}\mathbf{T}_{\mathbf{GB}}\mathbf{T}_{\mathbf{BE_0}}\mathbf{N}\right\} dV_{el} \tag{11}$$

$$\mathbf{C}^{\mathbf{el}} = 2\rho_e \int_{V_{el}} \left\{\mathbf{N}^{\mathbf{T}}\mathbf{T}_{\mathbf{BE_0}}^{\mathbf{T}}\mathbf{T}_{\mathbf{GB}}^{\mathbf{T}}\boldsymbol{\Omega}\mathbf{T}_{\mathbf{GB}}\mathbf{T}_{\mathbf{BE_0}}\mathbf{N}\right\} dV_{el} \tag{12}$$

$$\mathbf{K}_{\mathbf{d}}^{\mathbf{el}} = \rho_e \int_{V_{el}} \left\{\mathbf{N}^{\mathbf{T}}\mathbf{T}_{\mathbf{BE_0}}^{\mathbf{T}}\mathbf{T}_{\mathbf{GB}}^{\mathbf{T}}\left(\dot{\boldsymbol{\Omega}} + \boldsymbol{\Omega}\boldsymbol{\Omega}\right)\mathbf{T}_{\mathbf{GB}}\mathbf{T}_{\mathbf{BE_0}}\mathbf{N}\right\} dV_{el} \tag{13}$$

$$\begin{aligned}\mathbf{F}_{\mathbf{d}}^{\mathbf{el}} = \rho_e \int_{V_{el}} \{&\mathbf{N}^{\mathbf{T}}\mathbf{T}_{\mathbf{BE_0}}^{\mathbf{T}}\mathbf{T}_{\mathbf{GB}}^{\mathbf{T}}\ddot{\mathbf{X}}^{\mathbf{G}} + \mathbf{N}^{\mathbf{T}}\mathbf{T}_{\mathbf{BE_0}}^{\mathbf{T}}\mathbf{T}_{\mathbf{GB}}^{\mathbf{T}}\left(\dot{\boldsymbol{\Omega}} + \boldsymbol{\Omega}\boldsymbol{\Omega}\right)\mathbf{T}_{\mathbf{GB}}\mathbf{X}^{\mathbf{B}} \\ &+\mathbf{N}^{\mathbf{T}}\mathbf{T}_{\mathbf{BE_0}}^{\mathbf{T}}\mathbf{T}_{\mathbf{GB}}^{\mathbf{T}}\left(\dot{\boldsymbol{\Omega}} + \boldsymbol{\Omega}\boldsymbol{\Omega}\right)\mathbf{T}_{\mathbf{GB}}\mathbf{T}_{\mathbf{BE_0}}\mathbf{x_e}\}dV_{el}\end{aligned} \tag{14}$$

A 7-point Gauss quadrature is used for an integration of these terms. In addition, the total damping matrix includes the stiffness proportional damping.

C. Spring Element

Spring elements are used to provide additional stiffness to the triangular shell elements to analyze performances of highly flexible morphing wings in a fixed morphing shape. The spring element is a simple one-dimensional finite element where its coordinate coincides with the local coordinate of a corresponding triangular element. Two nodes

are assigned to describe each spring element. The stiffness of the spring element as shown in Fig. 2 can be expressed by k as [26]

$$k = \begin{bmatrix} k & -k \\ -k & k \end{bmatrix} \tag{15}$$

The stiffness components of the spring element are added to the ones of corresponding nodes in a triangular element in which the spring element is integrated.

Figure 2. Simple spring Element.

D. Time Integration of the Equations of Motion

The nonlinear structural equation of motion can be expressed as

$$\mathbf{Ma} + \mathbf{Cv} + \mathbf{Kd} = \mathbf{F} \tag{16}$$

where **M**, **C**, **K** are the global mass, damping (including the gyroscopic and stiffness proportional damping), and tangent stiffness matrices, which are assembled for the entire structures in the global frame, respectively. Also, **a**, **v**, **d** are the acceleration, velocity, and displacement vectors, respectively. The total force vector is denoted as **F**, which includes the external aerodynamic loads obtained by the UVLM. In the current work, the numerical integration of Eq. (16) is performed using the modified generalized-α improved for aeroelastic problems [27].

III. Numerical Studies

To verify the computations of matrices components in the dynamic equations of motion, a modal analysis performed by the developed nonlinear aeroelastic analysis framework and the solutions obtained by a commercial finite element analysis software MSC.Marc, which can provide geometrically nonlinear analysis, are compared. In addition, transient structural analysis solutions by the current code and MSC.Marc are also compared for verification purpose.

A. Verification of Modal Analysis

By using the global mass and stiffness matrices obtained in Eq. (16), a modal analysis can be performed. To verify the computations of the matrices in the current code, the result is compared with a solution obtained by MSC.Marc. A cantilever plate made of an isotropic material is modeled with 96 triangular shell elements. The material properties of the plate are Young's modulus E = 200 GPa, Poisson's ratio v = 0.29, and density ρ = 7850 kg/m^3. The geometries are thickness t = 0.1 m, length b = 16 m, width c = 1 m. The comparisons of the first and second out-of-plane bending modes are shown in Fig. 3. The natural frequency comparisons are listed in Table 1. It can be seen that the modal predictions show a very good agreement on the first and second bending modes.

B. Verification of Transient Structural Analysis

A time-domain dynamic analysis is performed to verify the implementation of the corotational approach with the extension for dynamic solutions. In the verification case, the above-mentioned isotropic plate is oscillated at the fixed root with a vertical sinusoidal acceleration of 0.1 m/s^2 at 1 Hz. Only the length is modified to 2 m, and the material properties are unchanged. The time integration parameters are time step n = 2,000 and dt = 0.001 s. Figure 4 shows a comparison result between solutions by the current code and MSC.Marc. The result shows an excellent agreement.

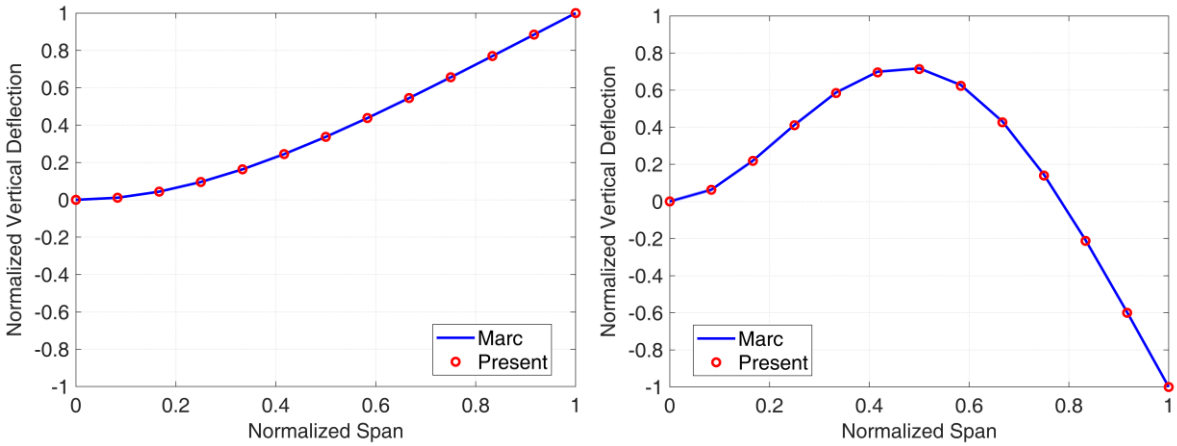

Figure 3. First (left) and second (right) bending mode.

Table 1. Natural frequencies.

Mode	Present	Marc
1st flatwise bending, Hz	0.32	0.32
2nd flatwise bending, Hz	2.02	2.04

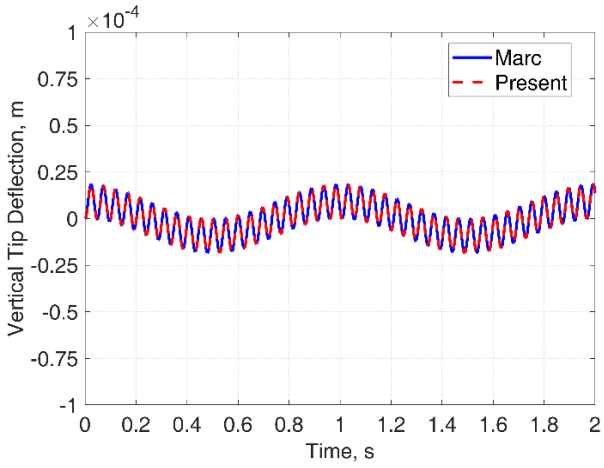

Figure 4. Vertical tip deflections over time.

C. Transient Solution of the Geometrically Nonlinear, Unsteady Aeroelastic Analysis

In this section, transient simulations with the geometrically nonlinear, unsteady aeroelastic analysis framework for a rectangular cantilever wing under a temporary external disturbance are presented to demonstrate the capability of the present analysis framework. The wing chord is 0.05 m and the semi-span is 1 m. The airfoil is NACA0012. The wing is made of an isotropic material with Young's modulus E = 200 GPa, Poisson's ratio ν = 0.29, and density ρ = 7850 kg/m^3. The wing is divided into 96 triangular shell elements. The free stream velocity U_∞ is 10 or 15 m/s, the altitude h is 500 m, and the wing root angle of attack α is 8°. The transient simulation duration following a static simulation is 2.4 s. The wing experiences a temporary disturbance for 1 s after reaching a steady-state flight condition. The external disturbance is sinusoidal (1-cosine) loads in the vertical upward direction with an amplitude of 50 N at U_∞ = 10 m/s and 80 N at U_∞ = 15 m/s at 2 Hz applied on all nodes of the wing. Figure 5 shows the external loads. The vertical deflections of the wing mid-chord from the transient simulations are shown in Fig.6. At the initial, the wing deflected due to steady-state aerodynamic loads. The wing then experienced medium and large deflections due to the external disturbances and came back to the steady-state conditions. Therefore, the present code successfully simulated problem involving the geometrical nonlinearity and the unsteady aerodynamics with different external loads and flow conditions. In a future work, to appropriately validate the analysis framework, experimental validations with wind tunnel tests will be performed.

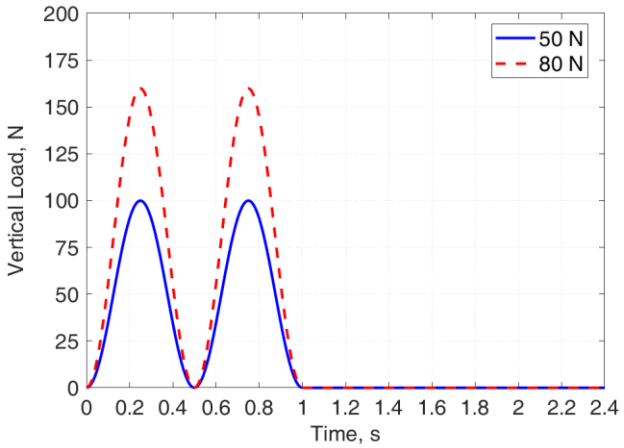

Figure 5. Sinusoidal external loads (frequency 2 Hz, amplitude 50 and 80 N).

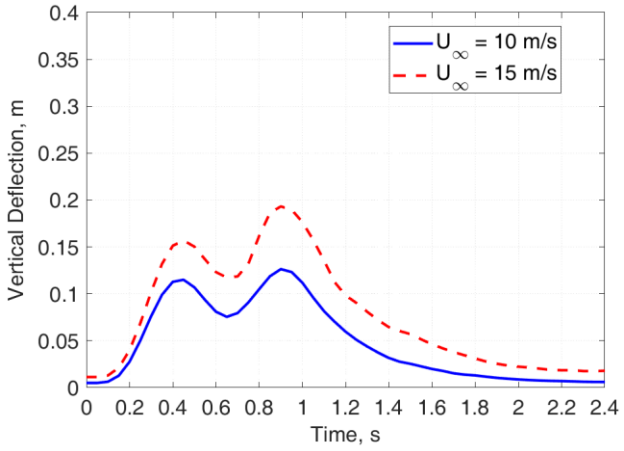

Figure 6. Wing tip vertical deflections at U_∞ = 10 and 15 m/s.

D. Aeroelastic Characteristics of Camber Morphing Wings with Corrugated Structures

To explore the aeroelastic characteristics of camber morphing wings with corrugated structures, a series of static aeroelastic simulations are performed in this section. Figure 7 shows the platform of the wing model. The tapered wing model is designed based on JAXA Technology Reference Aircraft (TRA) 2012A [28] and simplified for the following simulations. The wing root and tip chords are 5.103 m and 1.657 m, while the chord length between them are linearly interpolated. The semi-span length is 15.2 m and the aspect ratio is about 9. There is no sweep angle. In this study, NACA0012 is used for the airfoil shape. There are four trailing edge flaps (the flaps are denoted as "Flap1" and so on), and the length of each flap is 3.8 m. The wing is fixed at the wing root. For comparison purpose, two wings with different stiffnesses are evaluated. One is a rigid wing made of aluminum alloy A7075-T6, which has Young's modulus E = 71.7 GPa and Poisson's ratio ν = 0.33. The other is a flexible wing made of Nylon type 6/6, which has Young's modulus E = 28 GPa and Poisson's ratio ν = 0.4. The rigid wing would be a more realistic design, and it would provide a small (linear regime) deflection in higher speed subsonic flight. On the other hand, the flexible wing would experience large (nonlinear regime) deflection, which may provide a better understanding of wing's aeroelastic characteristics under large deformations. In addition, three different cases for each wing are simulated to evaluate the performance of camber morphing wings with corrugated structures, which are 1) no flap is deflected, 2) Flap 4 is replaced by a rotational hinged flap with 15°-deflection, 3) Flap 4 is replaced by a corrugated morphing flap with a similar deflection to the hinged flap. Figure 8 is an image of the hinged and corrugated flaps. The hinged flap is made of the same material as the main section of the wings. The corrugated morphing flap consists of flexible upper and lower skins and a round-corrugated structure to realize camber morphing. In the current study, it is assumed that structural properties of the flexible skins are negligible compared with the corrugated structure and the flexible skins only work to form smooth air flow. The corrugated structure is made of

the orthotropic material, IM7/8552. The material properties of IM7/8552 is given in Table 2. The ply angles of the laminate forming the corrugation are [0/90]s, and the thickness of the laminate is 7.32 mm. The wing model is divided into 12 elements in the spanwise direction and 10 elements in the chordwise direction, respectively. For the corrugated flap, the number of corrugation in a shell element is 3. To compare the performance of two types of flap, an approach in Ref. [29] is used. With this approach, the camber morphing flap is deflected so that the vertical deflection coincides with the one of the hinged flap with 15°-deflection for performance comparisons. Such a deflection is created by applying moments on the trailing edge of Flap 4 in the current study. Figure 9 shows the node locations of applied moments (the figure was created by MSC.Patran for a good visualization). The applied moments are 37.5 Nm on Node A, 77.2 Nm on Node B, 118 Nm on Node C, and 97 Nm on Node D about the *x* axis. The comparison of the wing tip shapes for the hinged and corrugated flaps obtained from a static analysis by the present code is shown in Fig. 10, in which "Corrugated (AL)" denotes the corrugated flap with the rigid main wing and "Corrugated (Nylon)" is the corrugated flap with the flexible main wing.

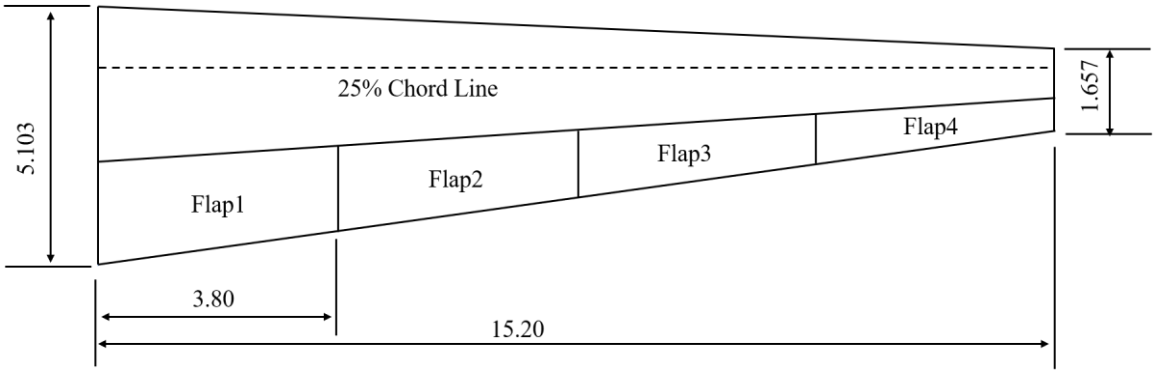

Figure 7. Wing planform.

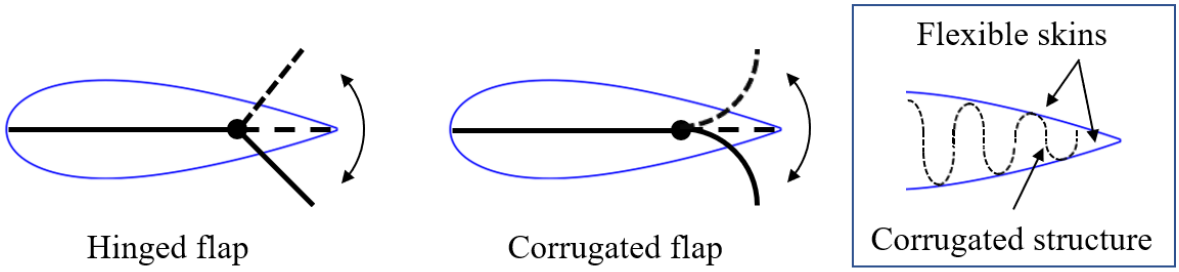

Figure 8. Hinged and corrugated morphing flaps.

Table 2. Material properties of IM7/8552.

Property	Value
Axial modulus E_1, GPa	171
Transverse modulus E_2, GPa	9.1
Poisson's ratio ν_{12}	0.32
Poisson's ratio ν_{23}	0.52
Shear modulus G_{12}, GPa	5.3
Shear modulus G_{23}, GPa	3.0

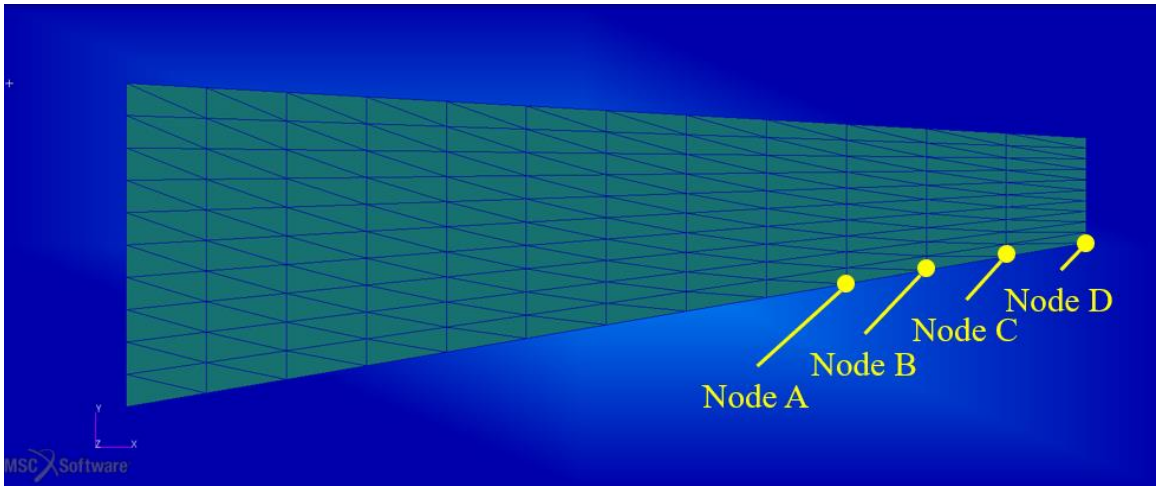

Figure 9. Node locations of applied moments.

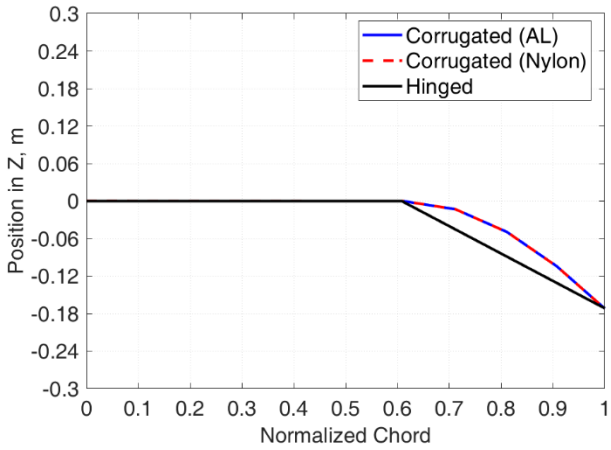

Figure 10. The outer tip deflection of the hinged and corrugated flaps.

Because the corrugated structures are very flexible in the corrugated direction, they require a certain mechanism to control/maintain the camber shape under loadings in actual applications. However, the current model does not consider such a control mechanism. Therefore, to fix the deflected shape for the following performance evaluations, rotational spring elements are added after the deflection shape of the corrugated flap on Flap 4 is determined. The spring element has a stiffness of 1×10^9 Nm/rad about the x axis as shown in Fig. 11.

In the following simulations, the free stream velocity U_∞ is 180 m/s, the altitude h is 500 m, and the wing root angle of attack α is 5°. Firstly, rigid wings with three flap configurations are simulated. Figure 12 shows the wing tip vertical deflections on the mid-chord line with the three configurations and the lift distributions on the trailing edge of Flap 4 with hinged and corrugated flaps. Both types of flap provided increased lift around the flaps resulting in the larger vertical deflections than the wing without any flap deflection. In addition, in the case of the aluminum alloy wings, the wing with the corrugated flap experienced a slightly larger vertical deflection than the wing with the hinged flap (5.13% larger at the wing tip) corresponding to larger lift around the flap (for example, the highest lift around the flap at the normalized span of 0.9 was increased by 118%).

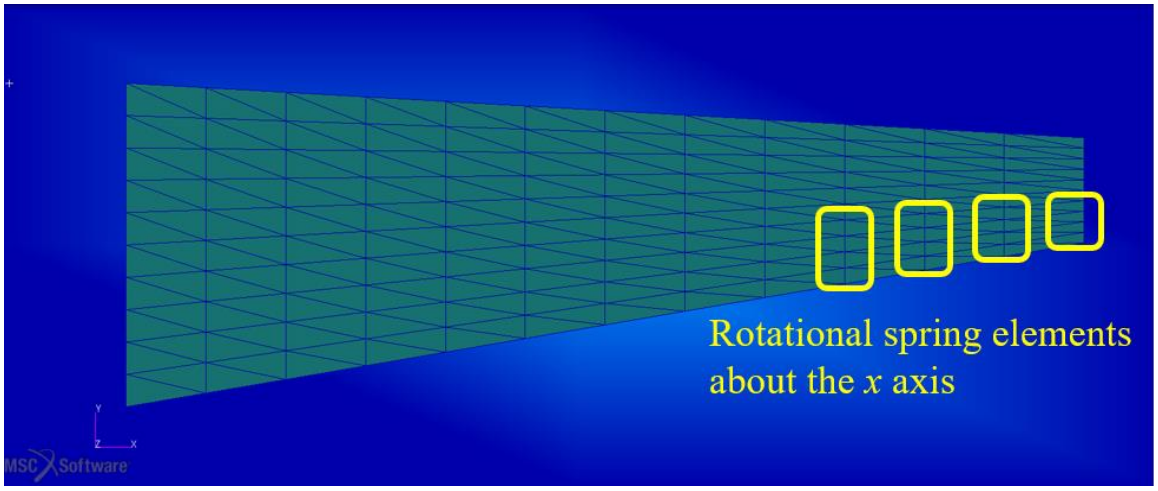

Figure 11. Locations of additional spring elements.

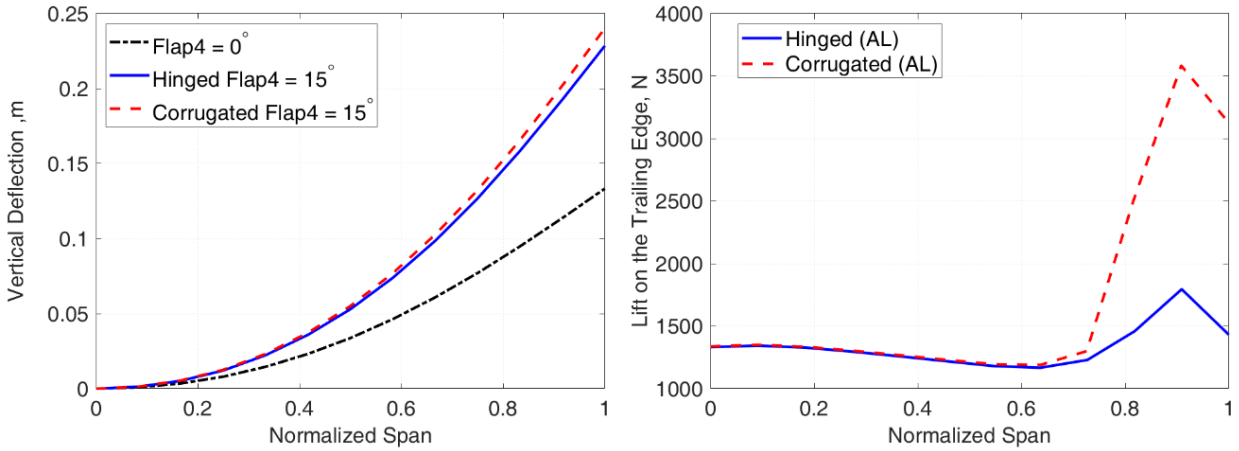

Figure 12. Wing tip vertical deflections on the mid-chord (left) and lift distributions on the trailing edge of Flap 4 with hinged and corrugated flaps for the rigid wings.

Next, flexible wings with three flap configurations are simulated. The results are shown in Fig. 13. In the case of flexible wings, the corrugated flap also provided larger lift forces (the lift at the normalized span of 0.9 was increased by 115%). On the other hand, the difference of the vertical deflections on the wings with deflected flaps is very small. This is attributed to the flexibility of the main section of the wing. The cross-sections of the wing tips of both wings with aluminum and nylon are plotted in Fig. 14. Although the flexible wing with the corrugated flap can generate larger lift, the main section of the flexible wing was twisted due to the large lift generated around the flap, which caused a reduction of effective local angle of attack. Consequently, the total lift of the flexible wing was reduced as can be seen in Fig.15. Figure 15 shows the distributions of chordwise summations of the elemental lift along the span for rigid and flexible wings. In the case of the rigid wing, the total lift was increased by 1.71%, while the total lift was decreased by 0.52% in the case of very flexible wing. Therefore, although the corrugated camber morphing can provide larger local lift, wing designs should be optimized by considering an overall balance of aeroelastic characteristics of wings with corrugated morphing flaps, especially in case of flexible wings.

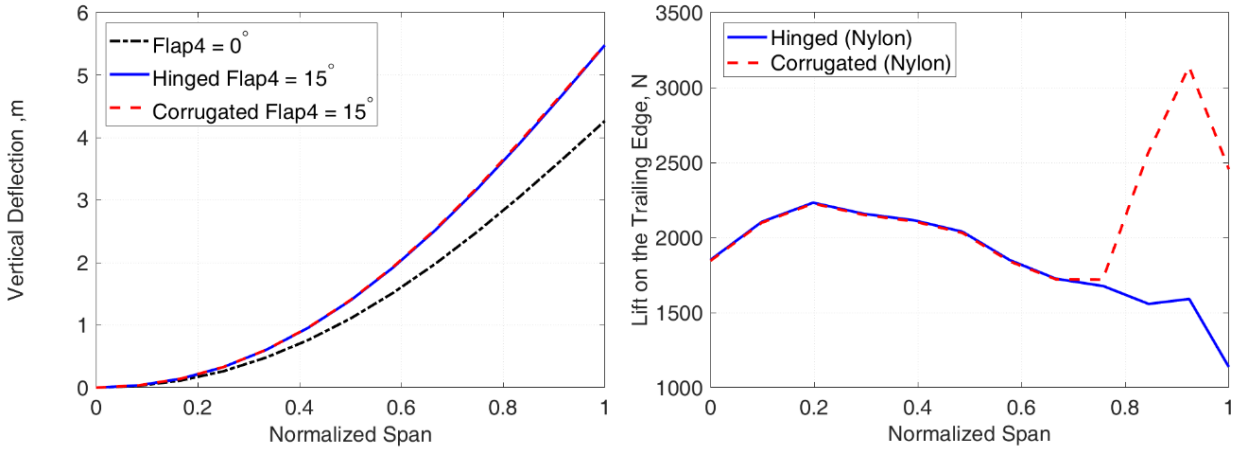

Figure 13. Wing tip vertical deflections on the mid-chord (left) and lift distributions on the trailing edge of Flap 4 with hinged and corrugated flaps for the flexible wings.

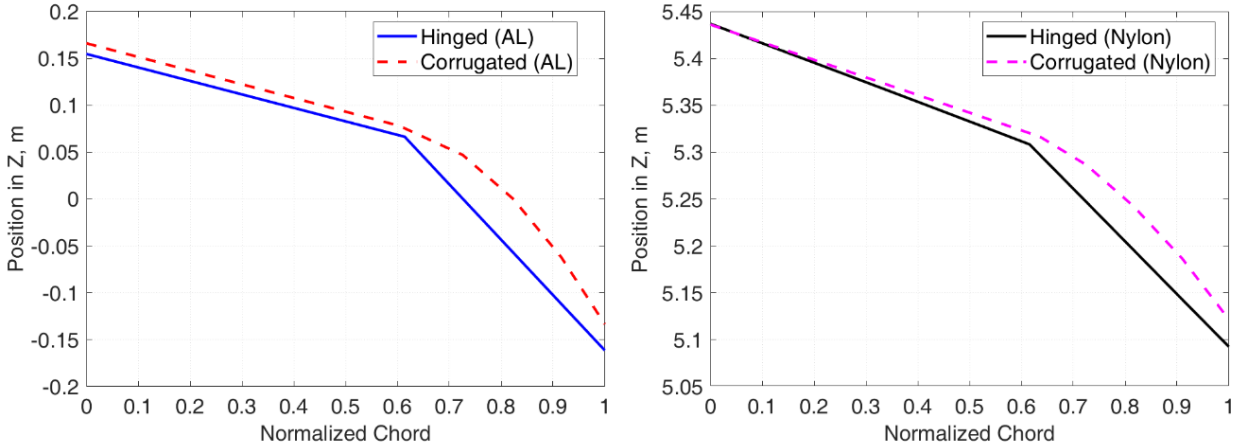

Figure 14. The cross-sections of the wing tips with aluminum alloy (left) and nylon (right).

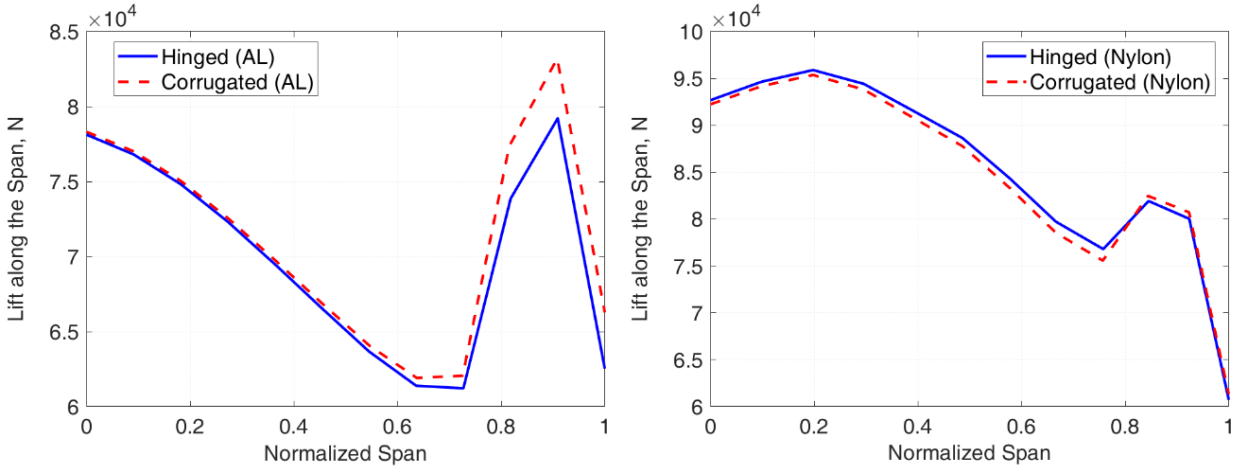

Figure 15. Distributions of chordwise summations of the elemental lift along the span for rigid (left) and flexible (right) wings.

IV. Conclusion

The objectives of this paper are to accommodate the integrated static aeroelastic analysis framework developed in the previous works for dynamic analysis to fully utilize the unsteady aerodynamic solver, and demonstrate the capability of the present analysis framework by exploring the aeroelastic characteristics of morphing wings with corrugated structures.

In the dynamic aeroelastic analysis framework, dynamic inertial effects are considered with the virtual work approach by taking into account the virtual work due to inertial forces. The time integration of the derived nonlinear structural equation of motion is performed by using the modified generalized-α improved for aeroelastic problems. In addition, the spring element is implemented in the structural solver for additional modeling capability, which helps to perform simple static aeroelastic analysis of the corrugated morphing wings. The verification of the mass matrix calculation was performed by comparing modal analysis solutions by the present code and MSC.Marc. The comparison showed good agreements between the solutions with respect to the lower bending mode shapes and natural frequencies. The time-domain structural dynamic analysis was also verified by comparing with the solution by MSC.Marc. There was an excellent agreement between the solutions as well.

The capability of the geometrically nonlinear, unsteady aeroelastic analysis framework was demonstrated through transient simulations with the analysis framework for a rectangular cantilever wing under a temporary external disturbance. The present code successfully simulated problems involving the geometrical nonlinearity and the unsteady aerodynamics although experimental validations with wind tunnel tests will be needed to appropriately validate the analysis framework.

To explore the aeroelastic characteristics of camber morphing wings with corrugated structures, a series of static aeroelastic simulations were performed. Tapered rigid and flexible wings with three different flap configurations, which were not deflected, hinged, and corrugated morphing flaps, were studied. The corrugated flap could provide a performance as a high-lift device. However, such local high-lift might create a different aeroelastic response to a wing and not always achieve the increase of total lift on a wing, especially in case of a flexible wing. Therefore, when a conventional hinged flap is replaced by a corrugated morphing flap, wing designs have to be optimized with respect to overall aeroelastic performance.

This work not only presented a better understanding of the nonlinear aeroelastic characteristics of composite and corrugated morphing wings, but also demonstrated the feasibility and capability of the methodology to simulate such morphing wings numerically. In future works, a detailed study of flexible skins such as effects of additional stiffness and vibrations of thin skins for the corrugated morphing wing will be performed for accurate investigations of morphing wing designs. In addition, a certain actuation mechanism to control/maintain morphing shapes, such as simple servo actuators or smart materials, will be designed and implemented for wing morphing actuation and control. A dynamic performance of a corrugated morphing wing with an actuation mechanism will also be studied to evaluate structural, aerodynamic, and control performance of such a wing.

References

1. Pendleton, E., Flick, P., Paul, D., Voracek, D. F., Reichenbach, E., and Griffin, K., "The X-53 A Summary of the Active Aeroelastic Wing Flight Research Program," *48th AIAA/ASME/ASCE/AHS/ ASC Structures, Structural Dynamics and Materials Conference and Exhibit*, Vol. AIAA Paper 2007-1855, AIAA Paper 2007-1855, Apr. 23-26, 2007.
2. Cumming, S. B., Smith, M. S., Ali, A., Bui, T. T., Ellsworth, J., and Garcia, C. A., "Aerodynamic Flight Test Results for the Adaptive Compliant Trailing Edge," *AIAA Atmospheric Flight Mechanics Conference*, AIAA Paper 2016-3855, AIAA Paper 2016-3855, Washington, DC, Jun. 13-17, 2016.
3. Smith, M. S., Bui, T. T., Garcia, C. A., and Cumming, S. B., "Longitudinal Aerodynamic Modeling of the Adaptive Compliant Trailing Edge Flaps on a GIII Aircraft and Comparisons to Flight Data," *AIAA Atmospheric Flight Mechanics Conference*, AIAA Paper 2016-3703, Washington, DC, Jun. 13-17, 2016.
4. Nguyen, N., Lebofsky, S., Ting, E., Kaul, U., Chaparro, D., and Urnes, J., "Development of Variable Camber Continuous Trailing Edge Flap for Performance Adaptive Aeroelastic Wing," *SAE 2015 AeroTech Congress and Exhibition*, SAE Technical Paper 2015-01-2565, SAE International, Seattle, WA, Sep. 22-24, 2015.
5. Kaul, U. K., and Nguyen, N. T., "Drag Optimization Study of Variable Camber Continuous Trailing Edge Flap (VCCTEF) Using OVERFLOW," *32nd AIAA Applied Aerodynamics Conference*, AIAA Paper 2014-2444, AIAA Paper 2014-2444, Atlanta, GA, Jun. 16-24, 2014.

6. Tsushima, N., and Su, W., "Concurrent Active Piezoelectric Control and Energy Harvesting of Highly Flexible Multifunctional Wings," *Journal of Aircraft*, Vol. 54, No. 2, 2016, pp. 724-736.
7. Tsushima, N., and Su, W., "Flutter suppression for highly flexible wings using passive and active piezoelectric effects," *Aerospace Science and Technology*, Vol. 65, 2017, pp. 78-89.
8. Tsushima, N., and Su, W., "Modeling of Highly Flexible Multifunctional Wings for Energy Harvesting," *Journal of Aircraft*, Vol. 53, No. 4, 2016, pp. 1033-1044.
9. Ortiz, P., and Alley, N., "Spanwise Adaptive Wing-PTERA Flight Test," NASA AFRC-E-DAA-TN57887, 2018.
10. Jackson, T., and Livne, E., "Integrated Aeroservoelastic Design Optimization of Actively Controlled Strain-Actuated Flight Vehicles," *AIAA Journal*, Vol. 52, No. 6, 2014, pp. 1105-1123.
11. Missoum, S., Dribusch, C., and Beran, P., "Reliability-Based Design Optimization of Nonlinear Aeroelasticity Problems," *Journal of Aircraft*, Vol. 47, No. 3, 2010, pp. 992-998.
12. Zuo, Y. T., Chen, P. J., Zhang, W., Li, C. H., Jiang, J. C., and Fan, F., "Rotor Airfoil Design Optimization Based on Unsteady Flow," *Transactions of the Japan Society for Aeronautical and Space Sciences*, Vol. 60, No. 6, 2017, pp. 366-377.
13. Livne, E., "Integrated aeroservoelastic optimization: Status and direction," *Journal of Aircraft*, Vol. 36, No. 1, 1999, pp. 122-145.
14. Tsushima, N., Su, W., Gutierrez, H., Wolf, M. G., Griffin, E. D., Whittaker, J. T., and Dumoulin, M. P., "Monitoring multi-axial vibrations of flexible rockets using sensor-instrumented reference strain structures," *Aerospace Science and Technology*, Vol. 71, 2017, pp. 285-298.
15. Yokozeki, T., Takeda, S., Ogasawara, T., and Ishikawa, T., "Mechanical properties of corrugated composites for candidate materials of flexible wing structures," *Composites Part a-Applied Science and Manufacturing*, Vol. 37, No. 10, 2006, pp. 1578-1586.
16. Takahashi, H., Yokozeki, T., and Hirano, Y., "Development of variable camber wing with morphing leading and trailing sections using corrugated structures," *Journal of Intelligent Material Systems and Structures*, Vol. 27, No. 20, 2016, pp. 2827-2836.
17. Yokozeki, T., Sugiura, A., and Hirano, Y., "Development of Variable Camber Morphing Airfoil Using Corrugated Structure," *Journal of Aircraft*, Vol. 51, No. 3, 2014, pp. 1023-1029.
18. Jung, Y. S., Yu, D. O., and Kwon, O. J., "Aeroelastic Analysis of High-Aspect-Ratio Wings Using a Coupled CFD-CSD Method," *Transactions of the Japan Society for Aeronautical and Space Sciences*, Vol. 59, No. 3, 2016, pp. 123-133.
19. Chimakurthi, S. K., Stanford, B. K., Cesnik, C. E., and Shyy, W., "Flapping wing CFD/CSD aeroelastic formulation based on a corotational shell finite element," *50th AIAA/ASME/ASCE/AHS/ASC Structures, Structural Dynamics, and Materials Conference*, AIAA Paper 2009-2412, Palm Springs, CA, May. 4-7, 2009.
20. Arizono, H., and Cesnik, C. E., "Computational Static Aeroelasticity Using Nonlinear Structures and Aerodynamics Models," *54th AIAA/ASME/ASCE/AHS/ASC Structures, Structural Dynamics, and Materials Conference*, AIAA Paper 2013-1862 Boston, MA, Apr. 8-11, 2013.
21. de Souza, C., da Silva, R. G., and Cesnik, C., "Nonlinear aeroelastic framework based on vortex-lattice method and corotational shell finite element," *53rd AIAA/ASME/ASCE/AHS/ASC Structures, Structural Dynamics and Materials Conference*, AIAA Paper 2012-1976, Honolulu, HI, Apr. 23-26, 2012.
22. Su, W., Huang, Y., and Hammerton, J. R., "Nonlinear Aeroelasticity of Highly Flexible Joined-Wing Aircraft using Unsteady Vortex-Lattice Method," *58th AIAA/ASCE/AHS/ASC Structures, Structural Dynamics, and Materials Conference*, AIAA Paper 2017-1353, Grapevine, TX, Jan. 9-13, 2017.
23. Tsushima, N., Yokozeki, T., Su, W., and Arizono, H., "Nonlinear Aeroelastic Analysis of Composite Morphing Wing with Corrugated Structures," *ASC 33rd Annual Technical Conference/ 18th US-Japan Conference on Composite Materials*, Sep. 24-26, 2018.
24. Chimakurthi, S. K., S. Cesnik, C. E., and Stanford, B. K., "Flapping-Wing Structural Dynamics Formulation Based on a Corotational Shell Finite Element," *AIAA Journal*, Vol. 49, No. 1, 2011, pp. 128-142.
25. Katz, J., and Plotkin, A., *Low-speed aerodynamics*, Cambridge University Press, Cambridge, UK, 2001.
26. Kattan, P. I., "The Spring Element," *MATLAB Guide to Finite Elements: An Interactive Approach*. Springer Berlin Heidelberg, Berlin, Germany, 2008, pp. 11-26.
27. Shearer, C., and Cesnik, C., "Modified generalized alpha method for integrating governing equations of very flexible aircraft," *47th AIAA/ASME/ASCE/AHS/ASC Structures, Structural Dynamics, and Materials Conference 14th AIAA/ASME/AHS Adaptive Structures Conference 7th*, 2006.

28. Kwak, D., Tamayama, M., Nomura, T., and Arizono, H., "Preliminary Studies on the Lift Distribution and Aspect Ratio of Subsonic Aircraft Wing for Fuel Consumption Reduction," *53rd JSASS Aircraft Symposium* JSASS, Toyama, Japan, 2015.
29. Sanders, B., Eastep, F. E., and Forster, E., "Aerodynamic and aeroelastic characteristics of wings with conformal control surfaces for morphing aircraft," *Journal of Aircraft*, Vol. 40, No. 1, 2003, pp. 94-99.